Supplementary Information (SI) for EES Batteries.

Understanding fast charging ability limitation in graphite electrode for Li-ion batteries.

Heterogeneities of lithiation in conventional electrodes.

Corentin Renais[a], Marta Mirolo[b], Victor Vanpeene[c], Maxime Servajon[a], Jakub Drnec[b], Fannie Alloin[a,*], Claire Villevieille[a,*]

a. *Univ. Grenoble Alpes, Univ. Savoie Mont Blanc, CNRS, Grenoble INP, LEPMI, Grenoble, France*

b. *ESRF, Experimental and Research Division, Grenoble, France*

c. *Université Grenoble Alpes, CEA, CNRS, IRIG, SyMMES, Grenoble, France*

Corresponding authors: fannie.alloin@grenoble-inp.fr; claire.villevieille@grenoble-inp.fr

Note 1 – Tortuosity factor determined by EIS

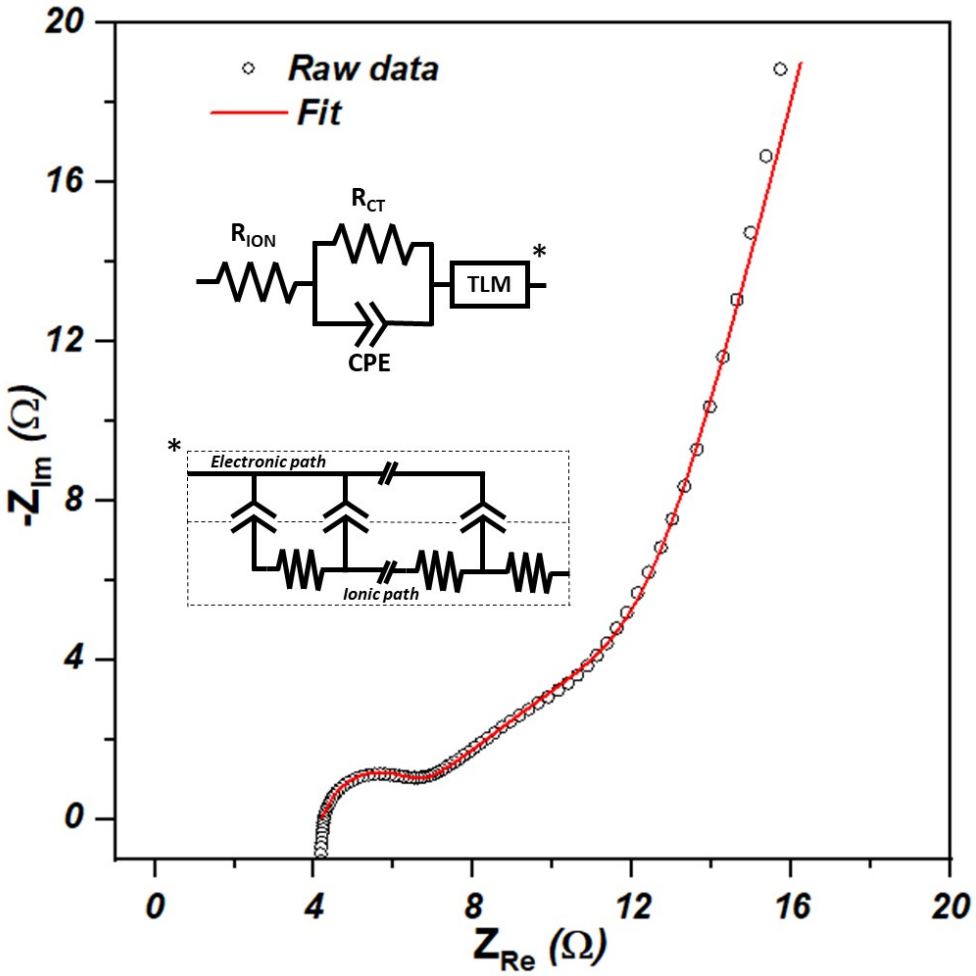

***Figure S1**. Electrochemical impedance spectrum of a symmetric cell composed of graphite electrodes with 50% porosity. Raw data are fitted using the equivalent circuit drawn, the asterisk gives the equivalent circuit the TLM-Q used.*

The impedance spectrum was fitted using the equivalent circuit given in **Figure S1**, the TLM-Q used to model the porous electrode is represented with the asterisk. The tortuosity is determined using the following **Equation a**:

$$\tau_{ion} = \frac{R_{ion}.A.\sigma_{ion}.\varepsilon}{d} \#(Eq.\ a)$$

With $R_{ion}\ (\Omega)$ the ionic resistance associated to ionic diffusion through the electrode porosity (half of the TLM-Q total resistance), A (cm^2) the cross-sectional area, σ_{ion} ($S.cm^{-1}$) the electrolyte ionic conductivity, ε the electrode porosity and d (cm) the electrode thickness.

Note 2 – Holotomography experiment (ID16b, ESRF)

The different phases were segmented from the reconstructed 8-bit ring-filtered volumes using a machine learning based random forest classifier embedded within the Ilastik software[1], and a combination of morphological filters. Theoretical values of porosities, estimated from the electrode loading, apparent density and thickness, have been used as guidelines for final images validation after segmentation selecting a threshold of probabilities higher than 0.85. The final images after segmentation for probabilities higher than 0.85 are presented in **Figure S2**. Globally, the results show errors that align with the intrinsic experimental noise along with localized error zones where large

binder domains are present. When the electrode is calendered, the uncertainty measured in these zones increase, because of the binder compaction and pore size decrease.

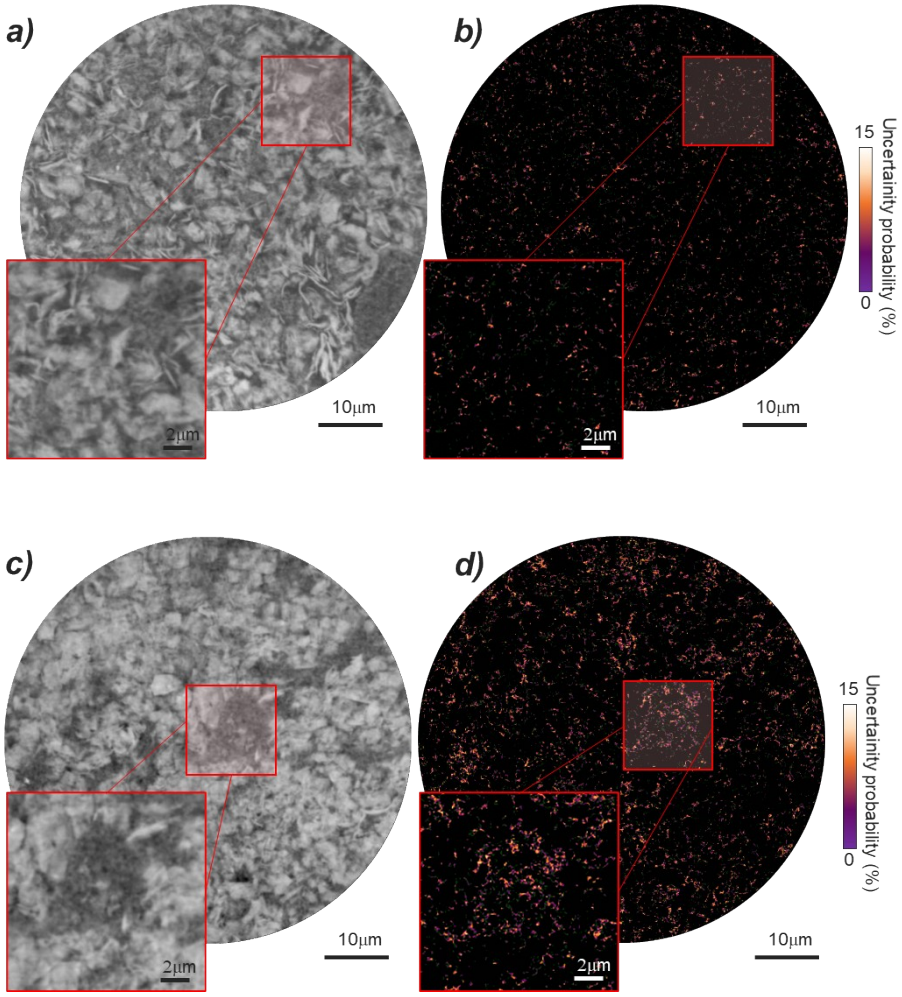

Figure S2. *(a,c) Reconstructed images in greyscale level and (b, d) corresponding uncertainty maps for a probability threshold set at 0.85 resulting from the random forest machine learning based segmentation for the (a, b) 50% and (c, d) 30 % porosity graphite electrode.*

Based on the same microstructural image data, flux maps were calculated through the reduction in diffusive transport caused by convolution in the geometry of heterogeneous media. This effect is captured in a term called the tortuosity factor τ, which is defined in the following equation (Eq.b):

$$D_{eff} = \frac{D\varepsilon}{\tau} \#(Eq.b)$$

where ε is the volume fraction of the ionic conductive phase; D its intrinsic diffusivity; and D_{eff} its effective diffusivity through a porous volume. The tortuosity factor τ is estimated by simulation while comparing the steady-state diffusive flow through a pore network with that through a fully dense control volume of the same size[2]. This steady-state diffusion problem satisfies the following set of equations, including the fixed Dirichlet conditions imposed at the two parallel boundaries identified thanks to their normal vector *n*.

$$\begin{cases} \nabla^2 C = 0 \\ \nabla C.n = 0 \\ C_{sep} = 1 \\ C_{cc} = 0 \end{cases} \#(Eq.c)$$

With C_{sep} and C_{cc} the salt concentration at the separator/electrode and electrode/collector interfaces.

Note 3 – Electrochemical formation cycle

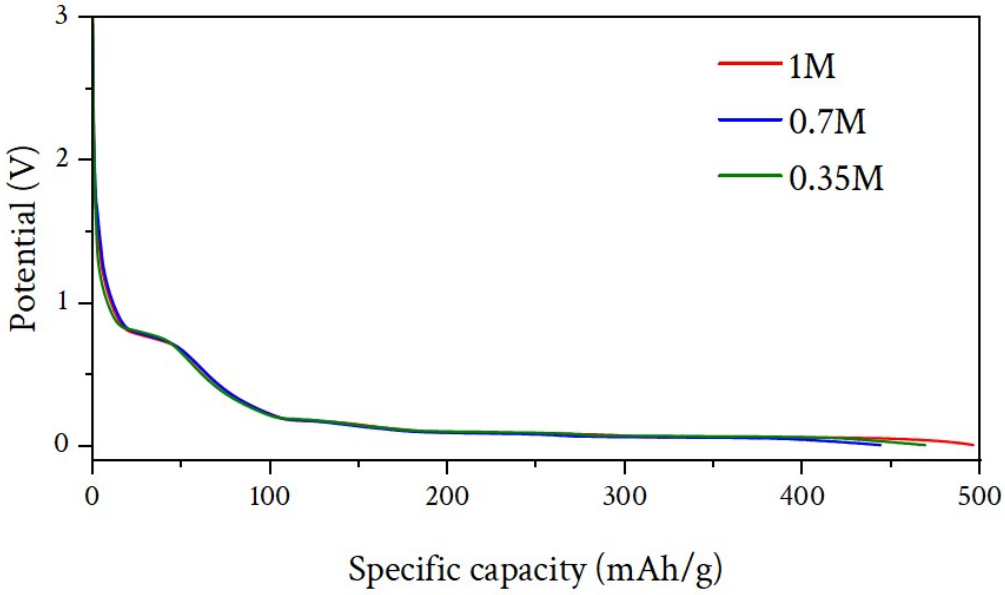

Figure S3*. First galvanostatic cycles of graphite vs. Li metal half-cells, cycled with different salt concentrations*

Note 4 – Porosity distribution

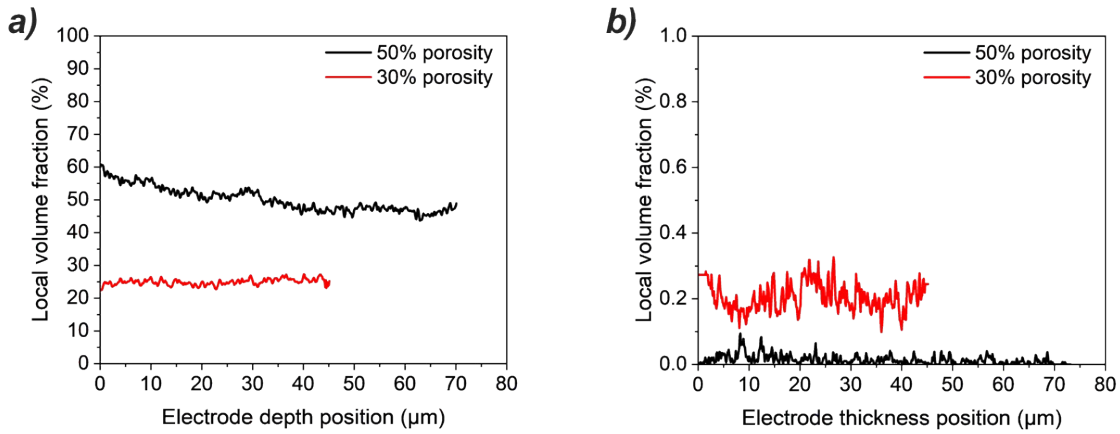

Figure S4*. Spatial distribution of a) the global porosity and b) the isolated pores along the electrode thickness. Note that 0 µm corresponds to the separator/electrode interface.*

Note 5 – In-plane and through-plane geodesic maps

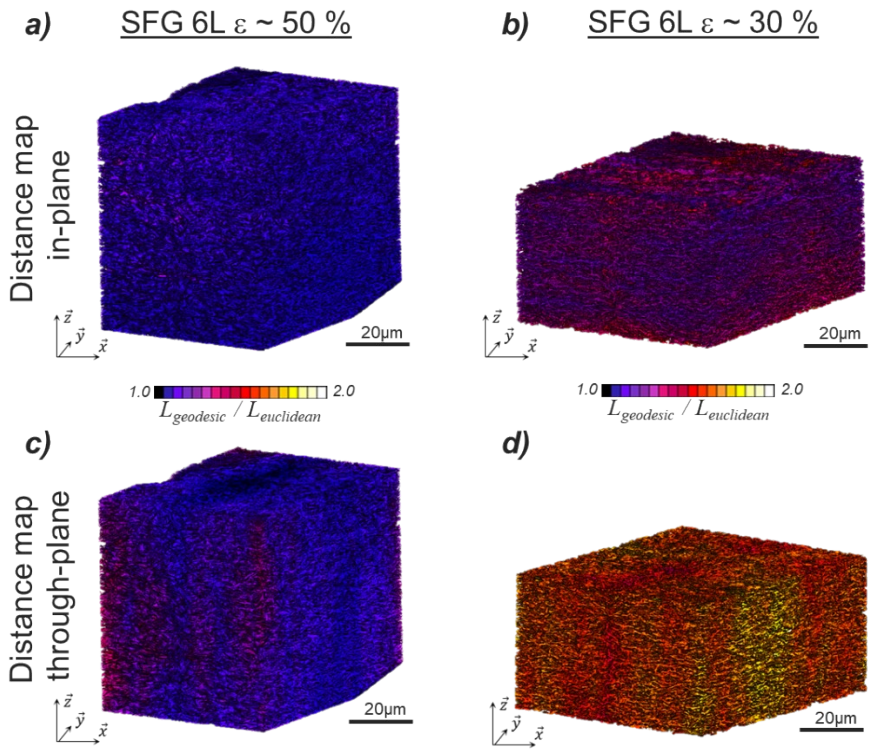

***Figure S5**. Distance maps for in-plane and through-plane geometrical tortuosity. In-plane orientation for a) 50% porosity and b) 30% porosity. Through-plane orientation for c) 50% porosity and d) 30% porosity.*

Note 6 – Structural state of charge estimation from model curve

An example of the diffraction patterns obtained during graphite electrode lithiation with 50% porosity at the positions near the separator (0.1 L) and near the current collector (0.9 L) are given in **Figure S6**. One can directly note a difference of structural evolution in the last biphasic domain, with a delay for the 0.9 L position.

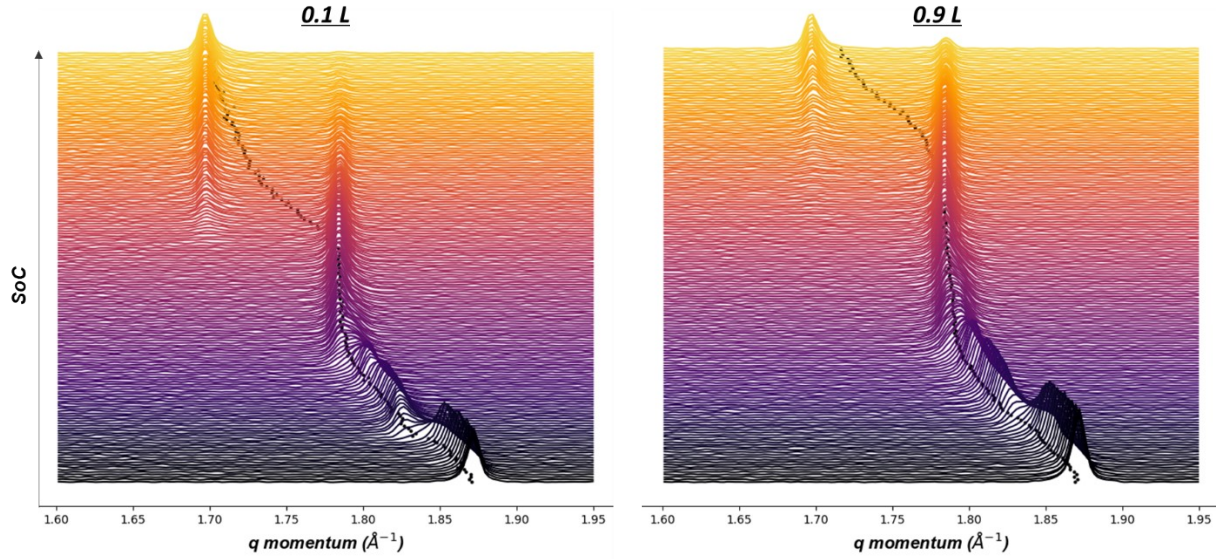

***Figure S6**. Evolution of diffraction pattern during graphite electrode lithiation with 50% porosity cycled at C/4 rate near the separator (0.1 L, left graph) and near the current collector (0.9 L, left graph). The black dotes under the diffraction patterns gives the mass center calculated as explained below.*

All the diffraction patterns recorded for the two porosities (50% and 30%) were treated using a mass centre calculation. A mean **q** scattering vector (*mc*) was calculated using a weighted arithmetic mean (**Eq. b**):

$$mc = \sum_{q_{min}}^{q_{max}} (I_q \times q) \Big/ \sum_{q_{min}}^{q_{max}} I_q \#(Eq.\ b)$$

Figure S7 shows the calculated mass center evolution with the SoC_{cell} for the two porosities at C/4 rate.

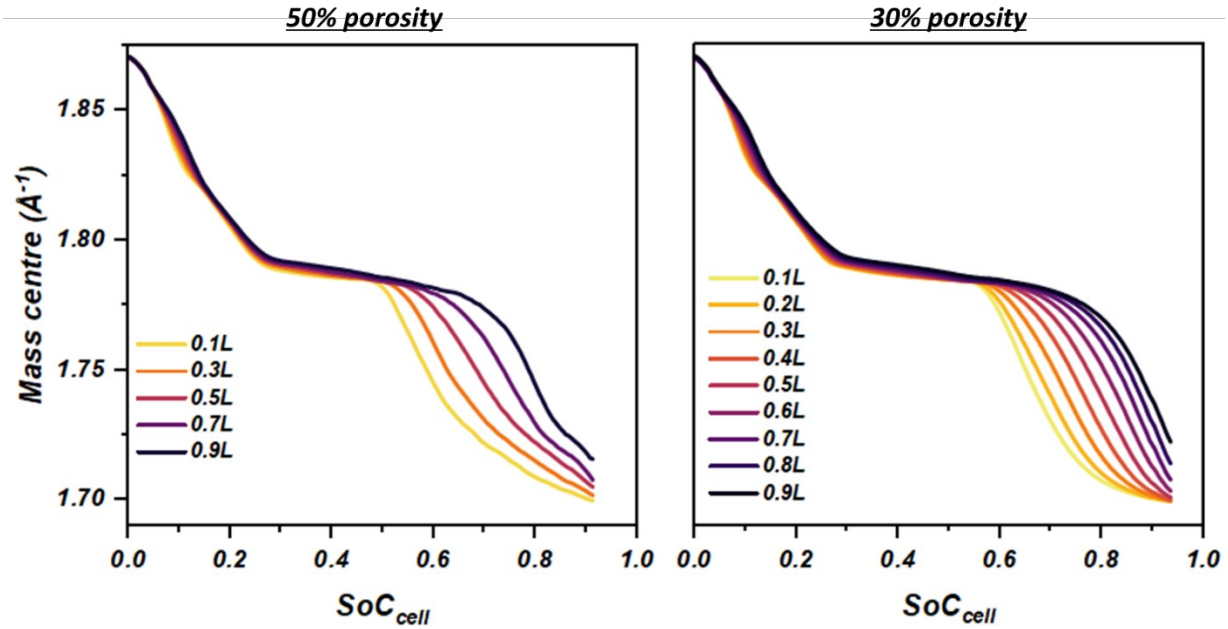

***Figure S7**. Mass center evolution at the different z-positions probed for the two electrode porosities at C/4 rate as a function of SoC_{cell}.*

From our previous publication [3], the mass centre evolution of the thin-film-like electrode upon lithiation (**Figure S8**) was used as a calibration profile to extract the structural state of charge (x in Li_xC_6) from the diffraction pattern obtained during this experiment at each position. A constant shift between the diffraction patterns of the thin-film-like electrode and the thick electrodes (50% and 30% porosity) is observed. To correct for this shift, the diffraction patterns were aligned based on specific peak positions such as pristine graphite, LiC_{12} and LiC_6 phases. The curve provided in **Figure S8** was then shifted by 0.011 $Å^{-1}$. In the end, the determined mass centres for both porosities (**Figure S7**) were translated to structural state of charge (*x* in Li_xC_6) based on this calibration curve.

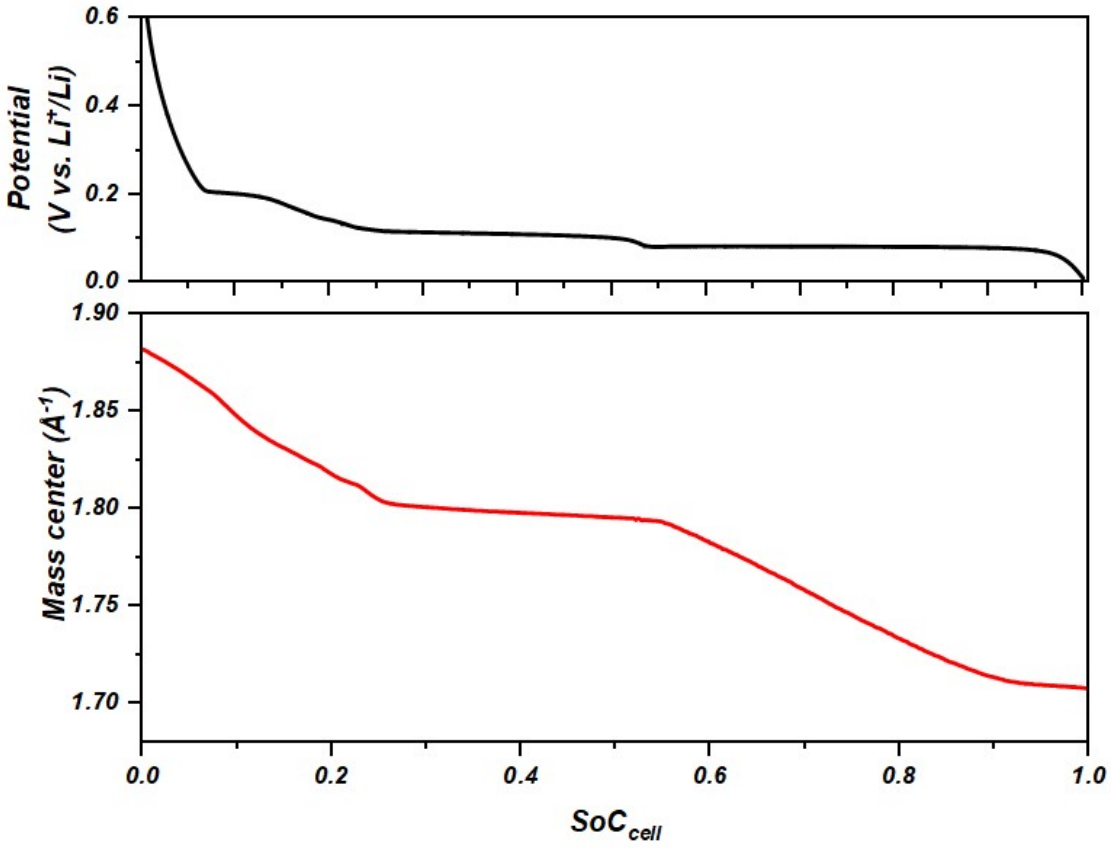

***Figure S8**. Model curve used for the determination of structural state of charge (x in Li_xC_6) from XRD patterns. a) Thin film electrode potential as a function of SoC_{cell}. b) Thin film electrode mass center evolution as a function of SoC_{cell}.* Note that with this thin-film configuration, one can assume a linear evolution between the structural (*x* in Li_xC_6) and electrochemical (SoC_{cell}) state of charge.

Note 7 – Comparison with another method in the determination of structural state of charge

To ensure that there is no artefact of data treatment on probed samples, we employed another method to determine the graphite state of charge (x in Li_xC_6) using the integrated signal of stage II and stage I (or stage I-enriched) peaks. Both phases were integrated to obtain the number of X-photons scattered by each phase. Similarly to the method using mass centre determination, we used the data from the thin-film-like electrode [4] to plot in **Figure S9a** the quasi-thermodynamic evolution of the proportion of stage I (or stage I-enriched) phase on the total integral with the SoC_{cell}. Using this model profile and the calculation procedure on the two electrode porosities of 50 and 30% (see **Figure S7b**), we were able to determine the structural state of charge with a second method (method 2). Note that this method is only valid for the stage II to stage I transition, and thus in the range ~0.5 – 0.9 SoC_{cell}.

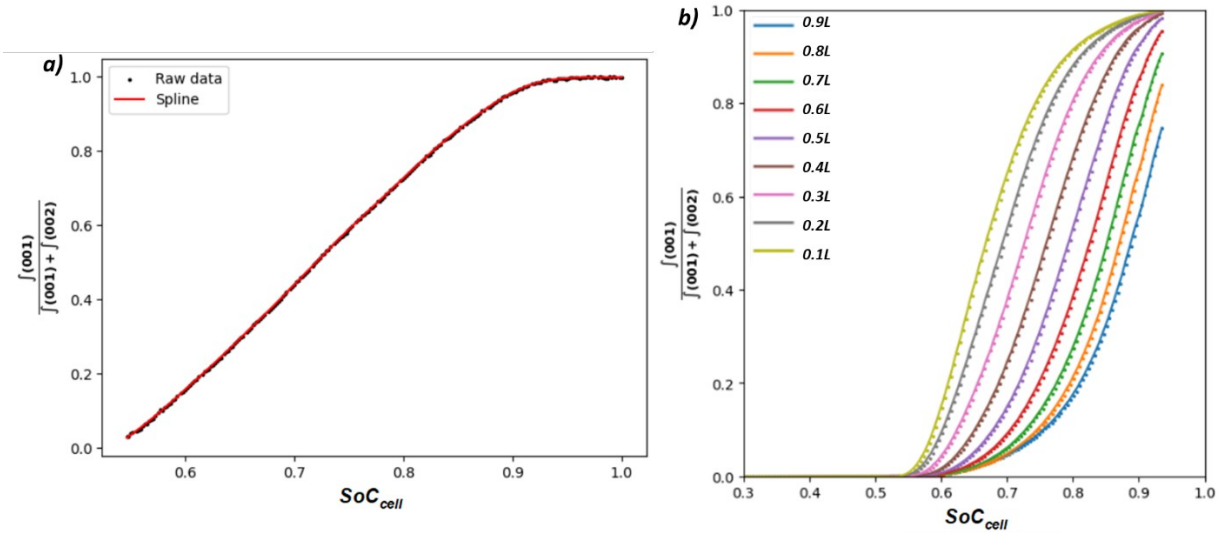

***Figure S9**. Fractional content of stage I (or stage I-enriched) phase over the total integral of X-photons scattered as a function of SoC_{cell}. a) Model profile obtained with the thin-film-like electrode. b) Results obtained with the thick electrode of 30% porosity cycled at C/4 rate for all the z-positions probed.*

Figure S10 compares the mean *x* in Li_xC_6 determined using the mass centre method (n°1, in black) and the integration method (n°2, in red) for the two electrode porosities cycled at C/4 rate. A very good agreement is found between the two methods used, strengthening the reliability of the results obtained with the mass centre determination.

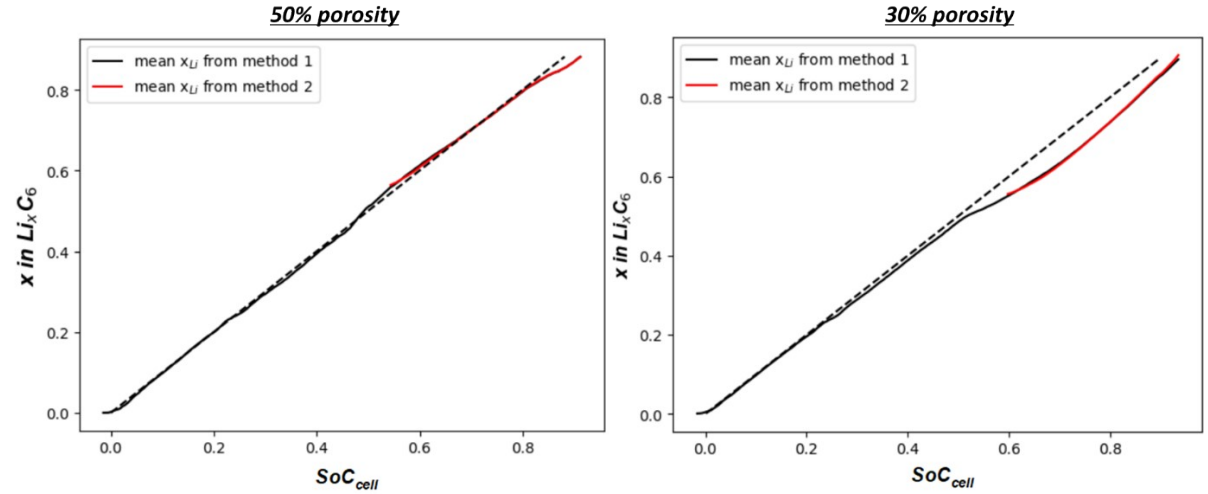

***Figure S10**. Comparison of the mean structural state of charge (x in Li_xC_6) determined using the mass centre method (1) and the integration method (2). Left for the 50% porosity electrode cycled at C/4 rate and right for the 30% porosity electrode cycled at C/4 rate. The dashed line corresponds to x = y.*

Note 8 – Nano dilatometry measurement performed on graphite electrode

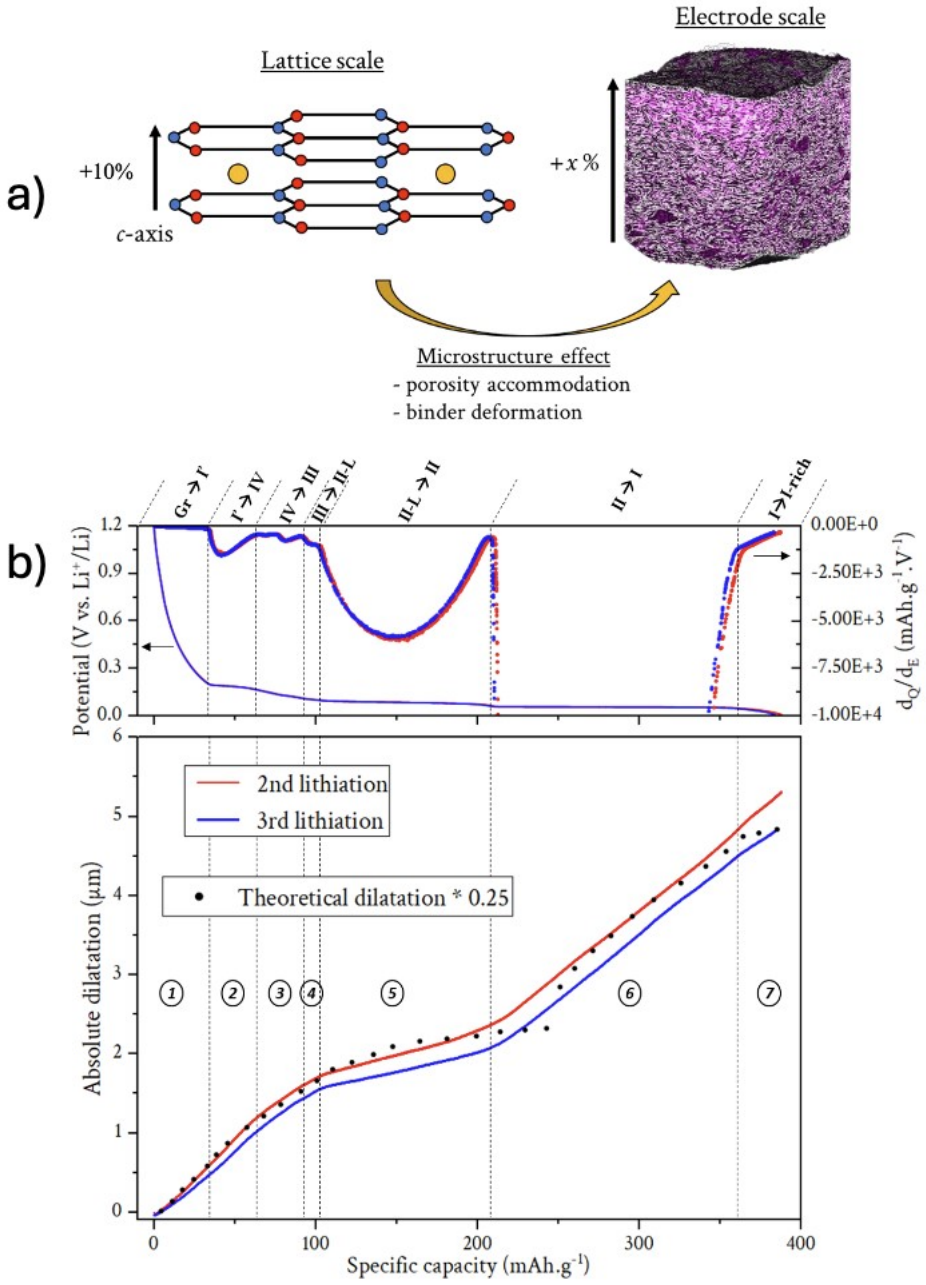

Figure S11. *a) Illustration of the link between dilatation at the lattice scale of graphite and at the electrode level; b) Second and third lithiation of a 70% porosity graphite electrode. a) Graphite electrode potential on the left axis, and the dQ/dE representation on the right axis. b) Absolute electrode dilatation initialised at zero (130 µm of initial thickness).*

Note 9 – AAD evolution with C-rate increase for the 30% porosity electrode

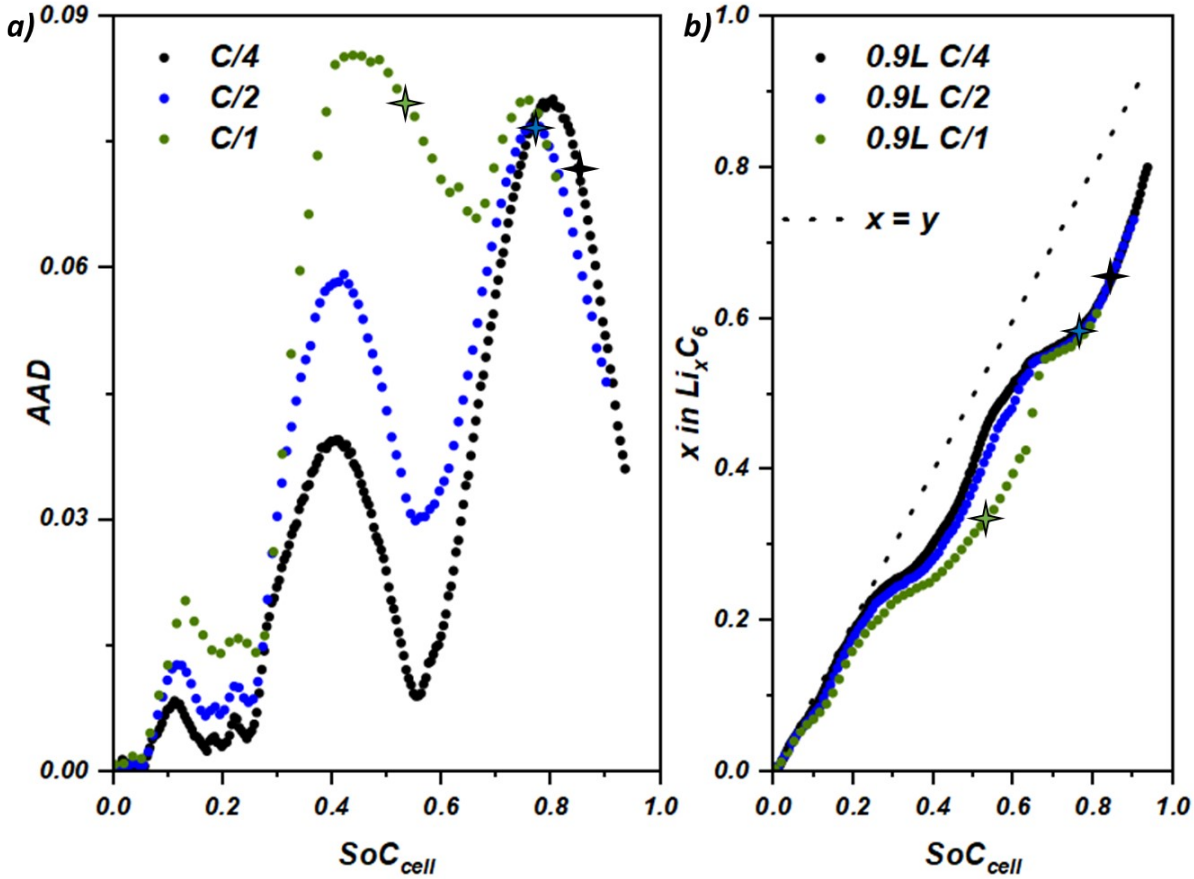

***Figure S12**. Evolution of structural state of charge (x in Li_xC_6) dispersion for 30% porosity graphite electrode at different cycling rates. a) Evolution of the AAD parameter as a function of SoC_{cell} for different cycling rates. b) Structural state of charge (x in Li_xC_6) evolution as a function of the SoC_{cell} at the 0.9 L position (near the current collector) for different cycling rates.*

Note 10 – Effective C-rate

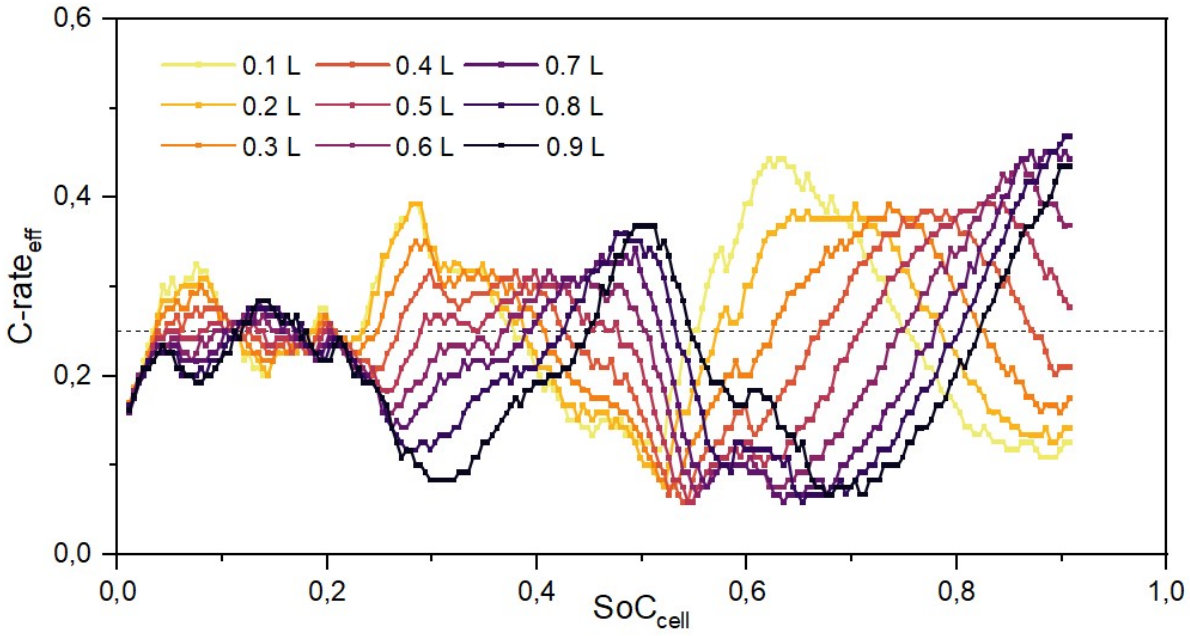

Figure S13 *: Evolution of the effective C-rate as a function of the cell state of charge for each z-position of the electrode of 30% porosity. The data correspond to the cycling at C/4.*

Note 11 – Effective C-rate distribution for the graphite electrode of 50% porosity

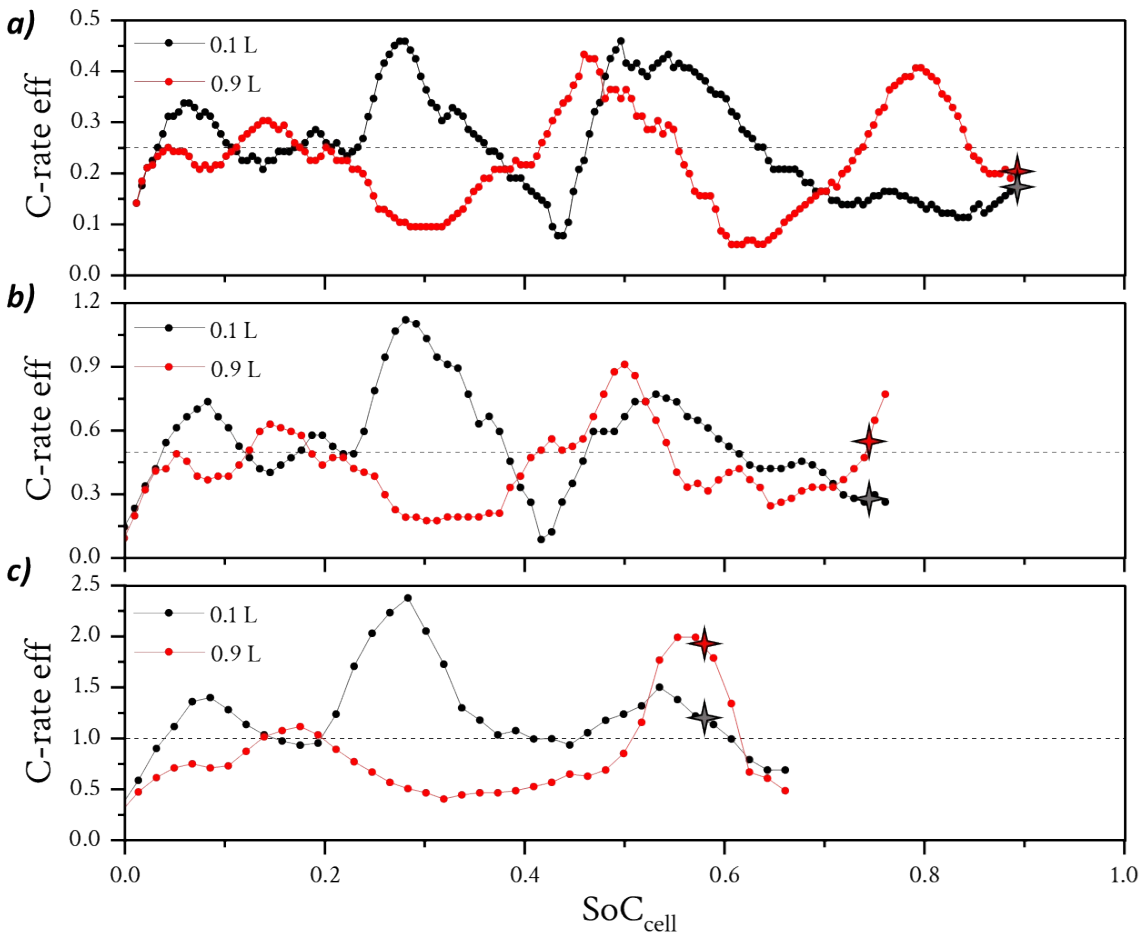

***Figure S14**. Evolution of effective C-rate as a function of SoC$_{cell}$ at the positions 0.1 L and 0.9 L for the graphite electrode of 50% porosity. a) Cycling rate of C/4, the dashed line at 0.25 corresponds to the applied C-rate at the cell level. b) Cycling rate of C/2. c) Cycling rate of C/1.*